nature geoscience

Article

https://doi.org/10.1038/s41561-023-01342-9

Palaeozoic cooling modulated by ophiolite weathering through organic carbon preservation

Received: 7 June 2023

Accepted: 26 October 2023

Published online: 30 November 2023

Check for updates

Joshua Murray & Oliver Jagoutz

Ophiolite obductions in the tropics are coeval with Phanerozoic glaciations. The exposure of mafic and ultramafic rocks is thought to trigger cooling by increasing global weatherability. However, each Palaeozoic icehouse also coincides with a $\delta^{13}C$ increase of 3–5‰, interpreted as an increase in organic carbon burial, not weatherability. Here we provide a framework that explains the tectonic forces behind Palaeozoic glaciations through increased organic carbon burial caused by the weathering of mafic and ultramafic lithologies in ophiolites. To evaluate the leverage ophiolite obduction has over organic carbon burial, we couple a mineral weathering model with a carbon box model. We show that the weathering of (ultra)mafic rocks can substantially enhance the preservation of organic carbon through the formation of high-surface-area smectite clays. The heightened organic carbon burial induced by an idealized ophiolite obduction causes ocean $\delta^{13}C$ to increase by ~3.7‰. The temporal evolution and magnitude of our modelled $\delta^{13}C$ excursion approximates Palaeozoic records. We present an analysis of shale geochemistry, which shows a correlation between ultramafic provenance and total organic carbon. Our results indicate that high-surface-area clays, formed during weathering of (ultra)mafic lithologies, exert a major control over Earth's long-term carbon cycle.

Earth's climate is primarily controlled by the partial pressure of carbon dioxide (p_{CO_2}) in the atmosphere[1]. The major tectonic control(s) of Earth's p_{CO_2} on million-year timescales are volcanic outgassing[2], silicate weatherability[3] and/or organic carbon (OC) burial[4]. The importance of mafic lithologies, uplift and local climate for chemical weathering has motivated recent studies that show a temporal coincidence between ophiolite obduction in the tropics and icehouse climates[5–8]. These studies argue that the obduction of mafic and ultramafic rocks (rich in Ca and Mg) raises Earth's weatherability, augmenting the flux of alkaline-earth cations to the ocean and increasing carbonate precipitation for a given p_{CO_2}.

The icehouse climates of the Palaeozoic era are characterized by positive excursions in records of $\delta^{13}C$, a signature of the enrichment of ^{13}C over ^{12}C (Methods). These records could be the result of weathering carbonate shelves following glacioeustatic marine regression[3]. Alternatively, heightened OC burial could simultaneously explain both global cooling and positive $\delta^{13}C$ through a single feedback[9,10] but has not been causally linked to the obduction of mafic and ultramafic lithologies in the tropics during times of glaciation[7,8].

Over 99.5% of all OC is degraded before it is buried below the upper reactive layer of marine sediment[11]. The fraction that is preserved is protected from remineralization by adsorption on the surface of clay minerals and iron oxides. As such, mineral species with high specific surface area (SSA) provide greater protection[12,13]. Shales rich in kaolinite, which has an SSA of 15 $m^2\,g^{-1}$, have systematically lower total organic carbon (TOC) levels than those rich in smectite, which has an SSA of ~800 $m^2\,g^{-1}$ (ref. 14) (Fig. 1e). As smectites are formed more readily under Mg-rich solutions and from Mg-rich bedrocks[15–18], we outline a

Department of Earth, Atmospheric, and Planetary Sciences, Massachusetts Institute of Technology, Cambridge, MA, USA. e-mail: joshmurr@mit.edu

https://doi.org/10.1038/s41561-023-01342-9

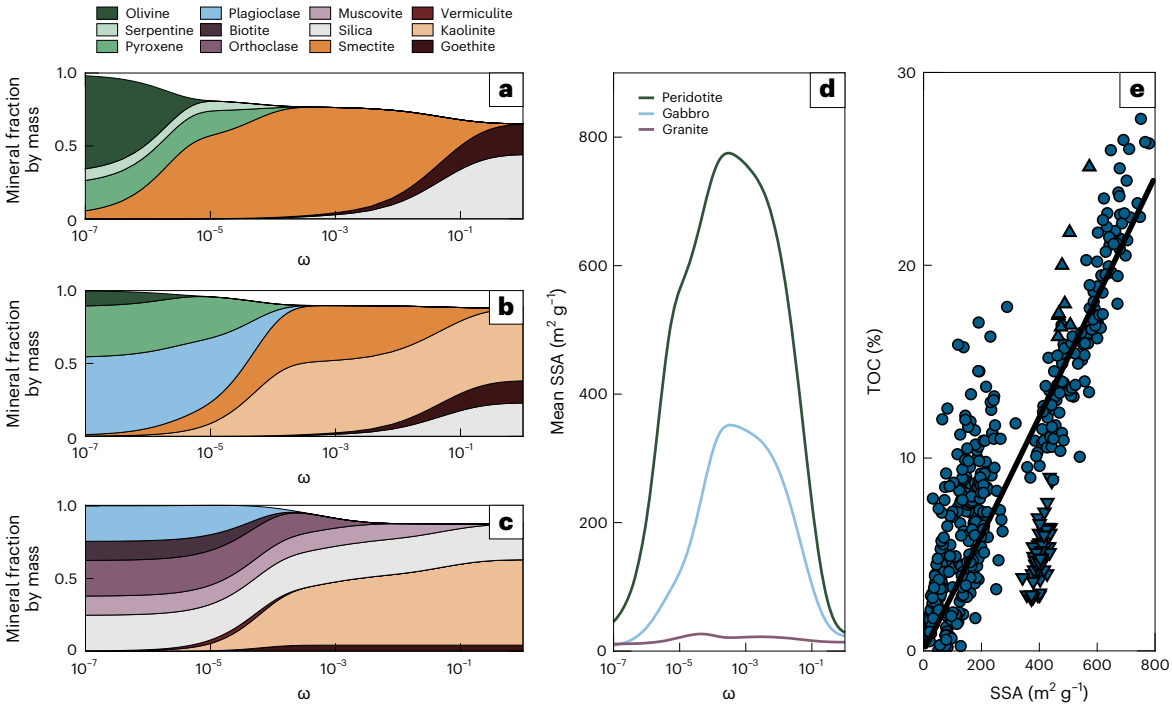

Fig. 1 | Relationships among primary lithology, modelled weathering products, SSA and TOC. a, Modelled weathering of peridotite (lherzolite) with 70% olivine, 20% pyroxene and 10% serpentine. **b**, Modelled weathering of gabbro with 60% plagioclase, 30% pyroxene and 10% olivine. **c**, Modelled weathering of granite with 25% plagioclase, 25% orthoclase, 12.5% muscovite, 12.5% biotite and 25% quartz. In panels **a**–**c**, mineral fraction is given as the fraction of the initial mass and progresses with increasing degree of weathering, ω (shown on a log scale). Relative weathering rates are given in Supplementary Table 1 (Methods). **d**, SSA of the bulk rock in panels **a**–**c** as the weathering reaction progresses. **e**, Compilation of SSA and TOC values. Downward-pointing triangles represent data in which the authors attribute TOC loss to bioturbation. Upward-pointing triangles represent data in which the authors document anoxia as contributing to high TOC values. The black line is a correlation consistent with monolayer equivalent adsorption of OC. We use this correlation to couple SSA to TOC (Methods). The same data are reproduced in Supplementary Fig. 1 differentiated by the sample location.

pathway by which (ultra)mafic rock exposures alter the long-term carbon cycle through enhanced OC preservation. We evaluate the effects of ophiolite-derived clays and subsequent OC burial, in tandem with increased weatherability, and reconcile Palaeozoic glaciations with changes in $\delta^{13}C$ and surface lithology.

Mineral weathering model

We present a simple model of clay formation through individual mineral weathering reactions. As fresh rocks are exposed on the surface, their constituent minerals chemically weather, first in situ and then during erosion and transportation to the continental shelf. The minerals formed during weathering and the rate of alteration depend upon the primary mineral, grain size, climate, microporosity and co-occurring mineralogy[19]. However, the ratio between mineral weathering rates remains approximately constant[20]. By using the most common reaction pathways and using relative reaction rates, we simplify weathering reactions of different lithologies to a tractable representation of clay formation (Methods).

We compiled the weathering reaction rates for eight common rock-forming minerals. Peridotite, gabbro and granite are treated as aggregates of their constituent minerals and serve as ultramafic, mafic and felsic endmembers, respectively. We tracked the mineralogy and SSA of each rock with increasing degree of chemical weathering, ω, (Fig. 1). Results of our model show that ultramafic rocks, and to a lesser extent mafic rocks, rapidly form smectite clays from their Al-poor primary minerals, leading to peak SSA (250–775 $m^2 g^{-1}$) sediments at $\omega = 10^{-3.6}$, before a decline in SSA as smectite is altered to silica and goethite with greater ω (Fig. 1). Felsic rocks weather more slowly due to their stable constituent minerals, and the resulting kaolinite-rich sediment has low SSA (14–27 $m^2 g^{-1}$), peaking around $\omega = 10^{-4.4}$ before vermiculite weathers to kaolinite (Fig. 1).

Carbon box model

The empirical relationship between SSA and TOC (Fig. 1e) provides a framework by which changes in lithology can force climate: mafic and ultramafic minerals create high-SSA clays that increase the preservation potential of OC. Irrespective of whether the OC is pedogenic or, more likely, marine in origin[21], its preservation in siliciclastic deposits represents a transfer of carbon from the ocean–atmosphere system to the lithosphere. We adopt a linear function to describe the influence of changing SSA on OC preservation and proceed to model the carbon-cycle response to a change in surface lithology using a simple one-box model that couples the global fraction of exposed felsic, mafic and ultramafic rocks to clay mineralogy (Fig. 1), silicate weathering flux, OC burial, ocean phosphorus and p_{CO_2}. We hold global sedimentation constant, and the silicate weathering flux refers to the mass of carbon sequestered as carbonates due to the chemical weathering of silicate minerals and the associated Ca and Mg released (Methods).

Ocean phosphorus is thought to play a critical role in OC burial through Earth history due to the limitations it places on primary productivity[22]. Over long timescales, if phosphorus is buried in organic matter according to the Redfield ratio, C/P of 106/1, OC burial cannot exceed the riverine flux of phosphorus, regardless of sedimentary SSA[22]. However, preferential recycling of phosphorus from the sediment back into the ocean has been well documented. In stratigraphic sections of organic-rich shales and anoxic conditions C/P ratios increase up to tenfold, including C/P in mineral-bound OC deposited during Ocean Anoxic Event 2 (refs. 23–26). Our model treats buried C/P ratio as a function of phosphorus in the ocean, and we present model results with differing maximum burial values of C/P (Methods). Our model is not intended to fully recreate the complexities

https://doi.org/10.1038/s41561-023-01342-9

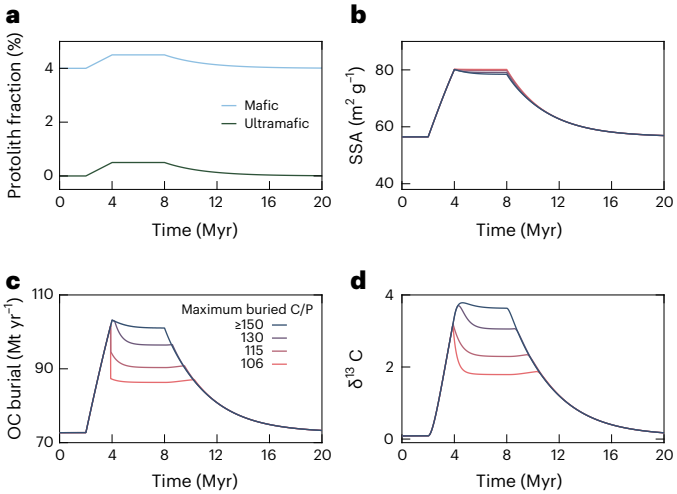

Fig. 2 | Model results from an idealized ophiolite obduction. Line colour reflects maximum C/P ratio in buried sediment (Methods). **a**, Fractions of mafic and ultramafic lithologies on Earth's surface. Felsic lithologies provide the remaining percentage. **b**, Mean SSA of silicate weathering products. **c**, Change in OC burial as a result of the increased average SSA **d**, Evolution of ocean $\delta^{13}C$ as OC burial changes.

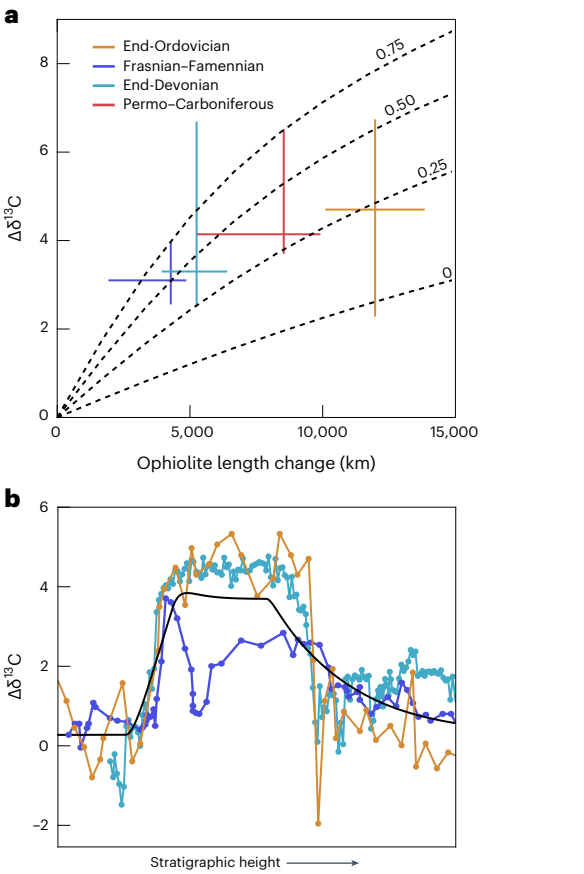

Fig. 3 | Comparison with the Palaeozoic $\delta^{13}C$ record. a, Magnitude of $\delta^{13}C$ excursions ($\Delta\delta^{13}C$) and changes in ophiolite length across the four Palaeozoic glaciations. The coloured lines reflect 1σ ranges of $\delta^{13}C$ excursions and ophiolite length changes. The intersection of the lines represents the median $\delta^{13}C$ excursion and ophiolite length change. Change in ophiolite length is derived from the sutures of ref. 8. Our compilation of $\delta^{13}C$ excursions (Supplementary Table 5 and Methods) is used to constrain the magnitude of $\delta^{13}C$ excursions across the end-Ordovician ($n = 10$), Frasnian–Famennian ($n = 8$) and end-Devonian ($n = 10$). The Permo–Carboniferous is not represented by a single stratigraphic section. Instead, we derive the size of the excursion from a comparison of brachiopod $\delta^{13}C$ values at the onset of the excursion ($n = 30$) with $\delta^{13}C$ values at the height of the excursion ($n = 70$) (ref. 10) (Methods and Supplementary Fig. 8). Black dashed lines are our modelled changes in ocean $\delta^{13}C$ as a function of the length and ultramafic fraction of the weathering ophiolite (0–0.75). **b**, Example $\delta^{13}C$ isotope excursions from the end-Ordovician, Frasnian–Famennian and end-Devonian glaciations using the same colour scheme as panel **a**[30–32]. Overlain in black is the modelled isotopic excursion without phosphorus limitation (Fig. 2d).

of the global carbon cycle, particularly the feedbacks that operate on short timescales, but rather to gauge the implications of increasing the fraction of siliciclastic sedimentation derived from mafic and ultramafic regions.

To approximate an ophiolite obduction, we forced the carbon box model by increasing the global surface fraction of ultramafic and mafic rocks by 0.5% each over 2 Myr from an initial 0% and 4%, respectively. This agrees with observed obduction length of 5,000 km and overthrust of 300 km (ref. 7). The influence of different obduction lengths and ultramafic fractions over steady-state $\delta^{13}C$ and p_{CO_2} is shown in Supplementary Figs. 2 and 3. To simulate the period over which tectonic uplift is equal to erosion, we maintained the amount of exposed ophiolite for 4 Myr, after which additional mafic and ultramafic lithologies decay exponentially (Fig. 2a).

In our model, the emplacement of mafic and ultramafic rocks results in a 61% increase in the mean SSA of global sediment from 56 $m^2\ g^{-1}$ to 80 $m^2\ g^{-1}$ (Fig. 2b). Assuming sufficient phosphorus recycling, the OC preservation associated with heightened SSA increases the OC burial flux from 73 MtC yr^{-1} to 102 MtC yr^{-1} (Fig. 2c). To reach steady state, p_{CO_2} decreases 3.7-fold (Supplementary Fig. 4c) until the silicate weathering flux decreases from 127 Mt yr^{-1} to 99 Mt yr^{-1}. This cooling lowers ω from 1.9×10^{-4} to 1.0×10^{-4}, which has a minor influence over SSA (Fig. 2b and Supplementary Fig. 4d). The OC burial causes a 3.7‰ positive $\delta^{13}C$ excursion (Fig. 2d). Using a climate sensitivity of 3–4 °C (ref. 27) yields mean global cooling of 6–8 °C, comparable to the changes observed at the initiation of icehouse climates[28]. Holding weatherability constant, making OC burial the sole driver of our carbon model, limits the p_{CO_2} decrease to 3.2-fold, corresponding to a 5–7 °C cooling (Supplementary Fig. 5).

If phosphorus is not recycled, OC burial becomes phosphorus-limited ~2 Myr after the onset of ophiolite obduction. This limitation is due to both a decrease in the riverine phosphorus flux as the silicate weathering flux decreases (Supplementary Fig. 6b) and an increase in OC burial (Fig. 2c). In this scenario, OC burial is capped at 86 Mt yr^{-1} by the riverine phosphorus flux. The isotopic excursion remains similar in magnitude, reaching 3.6‰, but is truncated by the phosphorus limitation, causing a rapid decrease in $\delta^{13}C$ to 1.8‰. The change in atmospheric p_{CO_2} is limited to a 2-fold decrease, which is reflected in both the silicate weathering flux and the degree of weathering, ω. We present intermediate values for maximum C/P of 106–150 in Fig. 2. For our obduction scenario, any buried C/P ratio greater than 142/1 yields identical model results for $\delta^{13}C$ and p_{CO_2} as the OC burial rate remains SSA-limited.

Alongside phosphorus, iron is thought to be a limiting nutrient in parts of the ocean[29]. However, these elements are more abundant in mafic lithologies than in felsic lithologies. Average mafic phosphorus concentrations are 1.5–2.0 times those of felsic rocks while mafic and ultramafic iron concentrations are 3.6 and 5.3 times those of felsic rocks, respectively (Supplementary Fig. 7). If scavenged in the nearshore environment, the high concentrations of essential nutrients in mafic rocks could serve to locally fertilize the ocean and further increase the burial of OC rather than limiting it. The impacts on the carbon cycle from combined ocean fertilization and OC preservation could be greater and more abrupt than is discussed herein.

https://doi.org/10.1038/s41561-023-01342-9

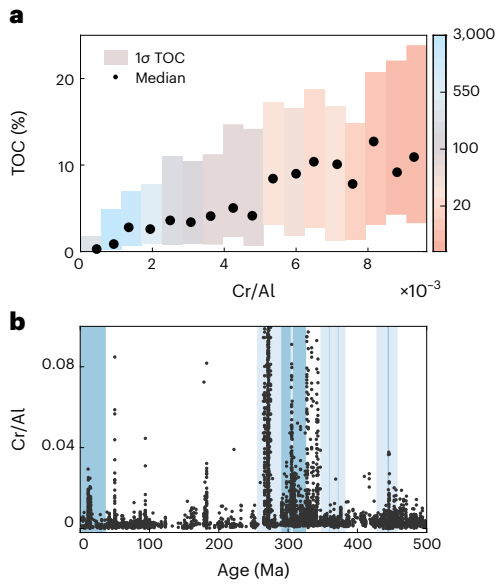

Fig. 4 | Analysis of SGP shale and siltstone geochemistries. a, Binned mean and standard deviation of SGP samples: horizontal axis is the ratio of Cr/Al, vertical axis represents TOC. Coloured boxes represent the single standard deviation of TOC for a given Cr/Al binned range. Black points show the median within the given bin. The colour of each rectangle denotes the number of samples contributing to the mean and standard deviation. At Cr/Al values exceeding 10^{-2}, the data are sparse and the relationship breaks down. This is probably caused by sorting, which concentrates chromite in coarser, clay-poor sediments. **b**, Cr/Al of SGP samples through the Phanerozoic overlain on Phanerozoic glaciations. Dark blue bars show short endmember chronologies of glaciation; pale blue bars show prolonged endmember chronologies (Methods and Supplementary Table 3). Data continue above the limits of the *y* axis, particularly around the Permo–Carboniferous.

Geologic and geochemical evidence

We compiled measured carbon isotopes across the four major Palaeozoic ice ages. The timing and extent of each glaciation is not well constrained (Methods) but is coeval with major ophiolite obductions[8] (Supplementary Fig. 8). We found that ophiolite obductions along longer suture zones coincide with greater $\delta^{13}C$ excursions (Fig. 3a). We show representative $\delta^{13}C$ excursions from carbonate sections for the end-Ordovician, Frasnian–Famennian and end-Devonian in Fig. 3b. The isotopic evolution is comparable to that of our model results, showing a rapid increase, a prolonged high $\delta^{13}C$ state, before a more gradual decline (Fig. 3b). The end-Ordovician is well preserved in carbonate stratigraphy in Nevada, showing a singular plateau of ~4‰ with a rapid onset and decrease[30] (Fig. 3b). The Frasnian–Famennian record consists of the two positive excursions of the lower and upper Kellewasser[31] (Fig. 3b). The negative $\delta^{13}C$ shift between the lower and upper Kellewasser horizons is qualitatively similar to our phosphorus-limited model. The end-Devonian has been sampled extensively by drill cores in Iowa where it resembles the end-Ordovician excursion in both magnitude and shape[32] (Fig. 3b). No single carbonate section captures the Permo–Carboniferous glaciation, which lasted at least 40 Myr and spanned multiple ophiolite obductions[8]. As such, we derived the magnitude of the excursion from a $\delta^{13}C$ fossil compilation[10] and added a spline fit with a smoothing parameter of 0.1 (Supplementary Fig. 8).

Isotopes of strontium and osmium have been used as proxies of silicate weathering. In both systems, mafic and ultramafic rocks are less radiogenic than their felsic counterparts with lower values of $^{87}Sr/^{86}Sr$ and $^{187}Os/^{188}Os$. Unfortunately, the Palaeozoic records of osmium are sparse, and those present are aliased due to their resolution being coarser than the ocean residence time of osmium (for example, refs. 33,34). Because the concentration of Sr in mafic and ultramafic rocks is lower than in felsic lithologies, coupling our silicate weathering rates to Sr fluxes predicts a minor $^{87}Sr/^{86}Sr$ decrease from 0.7083 to 0.7080, substantially smaller than the Palaeozoic variations (Methods and Supplementary Figs. 9 and 10). The change we infer from our model highlights the first-order control of strontium-rich continental rocks[35] and the inefficacy of $^{87}Sr/^{86}Sr$ as a diagnostic of ultramafic weathering. As Sr and Os weathering proxies are of limited use in evaluating our hypothesis, we used whole-rock geochemistry to assess the influence of ophiolite weathering over OC burial.

Our framework for lithologically induced glaciations makes a clear prediction for the sedimentary rock record: sediments dominantly sourced from (ultra)mafic rocks should, on average, have higher TOC than those derived from felsic lithologies. Chromium has long been used as a tracer of ultramafic provenance in sedimentary rocks[36,37] given its high concentration in the upper mantle[38] and relative immobility during weathering[39]. We examined the geochemistry of 7,820 shales, mudstones, and siltstones of the Sedimentary Geochemistry and Paleoenvironments Project (SGP) for which Cr, Al_2O_3 and TOC data are present[40]. We used Cr/Al ratios to remove the diluting effect of carbonate minerals. After discretizing the data, we observed a systematic increase in the median and range of shale TOC with increasing Cr/Al ratio (Fig. 4a and Methods). We then inspected the temporal variation in Cr/Al of the same SGP samples through the Phanerozoic and showed the heightened occurrence of high-Cr/Al samples during periods of glaciation (Fig. 4b). Median Cr/Al is 1.4 times greater, and the Cr/Al at the 97.5th percentile (2σ) is 4.2 times greater in shales deposited during glaciations compared with shales of warmer periods. Given its short 8 kyr residence time in the ocean[41], the Cr is probably derived from a proximal source rock, eroding essentially contemporaneously. The same trend is observed in Co/Al and Ni/Al, both insoluble trace elements that are concentrated in mantle peridotites relative to the continental crust (Supplementary Fig. 11). While the concentration of these elements in shales is additionally influenced by redox conditions and organic complexation, the fact that all three elemental ratios show similar trends supports our interpretation of an ultramafic signature. This correlation could be further bolstered by analysis of organo–mineral interfaces in Plio–Pleistocene sediments where an increase in detritus from the ultramafic terranes of the Southeast Asian islands ~4 million years ago is concurrent with an increase in TOC from 0.2–0.5 wt% to 1.0–1.8 wt% (refs. 42,43).

A TOC value greater than ~15%, as observed in Fig. 4a, may be greater than can be adsorbed to mineral surfaces and requires a combination of both high SSA and an anoxic environment[44]. Even ignoring those data exceeding 15 wt% TOC, the sedimentary geochemistry supports the observation that the shales with a larger ultramafic component, on average, preserve a greater fraction of OC and that those shales occur more frequently during glacial periods (Fig. 4 and Supplementary Fig. 11).

Alongside the geochemical correlation in Fig. 4, we see evidence of ultramafic detritus (notably Cr-spinel) and slab break-off closely preceding each Palaeozoic glaciation (Supplementary Figs. 12–14). Although Cr-spinel provides direct evidence of ophiolite weathering, slab processes may be governing the transport of high-SSA clays. While we treat ω as a global value, dependent upon only temperature, ω is high in areas with high chemical-weathering rates and low erosion rates, where thick regoliths develop and smectite clays are further altered into iron oxides[5,16]. Slab break-off would cause rapid uplift, enhanced erosion, lower ω and an increase in high-SSA sedimentation. The positive feedbacks among uplift, weathering and erosion may cause punctuated cooling on timescales much faster than plate convergence.

In summary, through the framework of OC burial, we reconcile the theory of ophiolite-induced cooling with carbon isotope excursions across Palaeozoic glaciations. Our model calculations, the $\delta^{13}C$ isotopic record and shale geochemistry all provide evidence to support the hypothesis that OC preservation by high-SSA clays is a major pathway

by which ophiolite obduction disrupts the carbon cycle. The influence of tectonically driven clay formation and subsequent increased OC preservation could extend far beyond Phanerozoic p_{CO_2} and be relevant for ocean anoxia, great oxidation event(s), and the initiation of snowball Earth[24,45,46].

Online content

Any methods, additional references, Nature Portfolio reporting summaries, source data, extended data, supplementary information, acknowledgements, peer review information; details of author contributions and competing interests; and statements of data and code availability are available at https://doi.org/10.1038/s41561-023-01342-9.

References

1. Owen, T., Cess, R. D. & Ramanathan, V. Enhanced CO_2 greenhouse to compensate for reduced solar luminosity on early Earth. *Nature* **277**, 640–642 (1979).
2. McKenzie, N. R. et al. Continental arc volcanism as the principal driver of icehouse–greenhouse variability. *Science* **352**, 444–447 (2016).
3. Kump, L. R. et al. A weathering hypothesis for glaciation at high atmospheric p_{CO_2} during the Late Ordovician. *Palaeogeogr. Palaeoclimatol. Palaeoecol.* **152**, 173–187 (1999).
4. Galy, V. et al. Efficient organic carbon burial in the Bengal fan sustained by the Himalayan erosional system. *Nature* **450**, 407–410 (2007).
5. Dessert, C., Dupré, B., Gaillardet, J., François, L. M. & Allegre, C. J. Basalt weathering laws and the impact of basalt weathering on the global carbon cycle. *Chem. Geol.* **202**, 257–273 (2003).
6. West, A. J., Galy, A. & Bickle, M. Tectonic and climatic controls on silicate weathering. *Earth Planet. Sci. Lett.* **235**, 211–228 (2005).
7. Jagoutz, O., Macdonald, F. A. & Royden, L. Low-latitude arc–continent collision as a driver for global cooling. *Proc. Natl Acad. Sci. USA* **113**, 4935–4930 (2016).
8. Macdonald, F. A., Swanson-Hysell, N. L., Park, Y., Lisiecki, L. & Jagoutz, O. Arc–continent collisions in the tropics set Earth's climate state. *Science* **364**, 181–184 (2019).
9. Kump, L. R. & Arthur, M. A. Interpreting carbon-isotope excursions: carbonates and organic matter. *Chem. Geol.* **161**, 181–198 (1999).
10. Grossman, E. L. et al. Glaciation, aridification, and carbon sequestration in the Permo–Carboniferous: the isotopic record from low latitudes. *Palaeogeogr. Palaeoclimatol. Palaeoecol.* **268**, 222–233 (2008).
11. Hedges, J. I. & Keil, R. G. Sedimentary organic matter preservation: an assessment and speculative synthesis. *Mar. Chem.* **49**, 81–115 (1995).
12. Lalonde, K., Mucci, A., Ouellet, A. & Gélinas, Y. Preservation of organic matter in sediments promoted by iron. *Nature* **483**, 198–200 (2012).
13. Hemingway, J. D. et al. Mineral protection regulates long-term global preservation of natural organic carbon. *Nature* **570**, 228–231 (2019).
14. Kennedy, M. J., Pevear, D. R. & Hill, R. J. Mineral surface control of organic carbon in black shale. *Science* **295**, 657–660 (2002).
15. Harder, H. The role of magnesium in the formation of smectite minerals. *Chem. Geol.* **10**, 31–39 (1972).
16. Nahon, D., Colin, F. & Tardy, Y. Formation and distribution of Mg, Fe, Mn-smectites in the first stages of the lateritic weathering of forsterite and tephroite. *Clay Miner.* **17**, 339–348 (1982).
17. Brigatti, M. F. & Poppi, L. 'Corrensite-like minerals' in the Taro and Ceno valleys, Italy. *Clay Miner.* **19**, 59–66 (1984).
18. Obeso, de, Carlos, J. & Kelemen, P. B. Major element mobility during serpentinization, oxidation and weathering of mantle peridotite at low temperatures. *Phil. Trans. R. Soc. A* **378**, 20180433 (2020).
19. Velde, B. B. & Meunier, A. *The Origin of Clay Minerals in Soils and Weathered Rocks* (Springer, 2008).
20. Velbel, M. A. Constancy of silicate-mineral weathering-rate ratios between natural and experimental weathering: implications for hydrologic control of differences in absolute rates. *Chem. Geol.* **105**, 89–99 (1993).
21. Blattmann, T. M. et al. Mineralogical control on the fate of continentally derived organic matter in the ocean. *Science* **366**, 742–745 (2019).
22. Laakso, T. A. & Daniel, P. S. Regulation of atmospheric oxygen during the Proterozoic. *Earth Planet. Sci. Lett.* **388**, 81–91 (2014).
23. Li, Y., Zhang, T., Ellis, G. S. & Shao, D. Depositional environment and organic matter accumulation of Upper Ordovician–lower Silurian marine shale in the Upper Yangtze Platform, South China. *Palaeogeogr. Palaeoclimatol. Palaeoecol.* **466**, 252–264 (2017).
24. Percival, L. M. E. et al. Phosphorus-cycle disturbances during the Late Devonian anoxic events. *Glob. Planet. Change* **184**, 103070 (2020).
25. Beil, S. et al. Cretaceous oceanic anoxic events prolonged by phosphorus cycle feedbacks. *Climate* **16**, 757–782 (2020).
26. Löhr, S. C. & Kennedy, M. J. Organomineral nanocomposite carbon burial during Oceanic Anoxic Event 2. *Biogeosciences* **11**, 4971–4983 (2014).
27. Sherwood, S. C., Bony, S. & Dufresne, J.-L. Spread in model climate sensitivity traced to atmospheric convective mixing. *Nature* **505**, 37–42 (2014).
28. DeConto, R. M. et al. Thresholds for Cenozoic bipolar glaciation. *Nature* **455**, 652–656 (2008).
29. Moore, C. M. et al. Processes and patterns of oceanic nutrient limitation. *Nat. Geosci.* **6**, 701–710 (2013).
30. LaPorte, D. F. et al. Local and global perspectives on carbon and nitrogen cycling during the Hirnantian glaciation. *Palaeogeogr. Palaeoclimatol. Palaeoecol.* **276**, 182–195 (2009).
31. Buggisch, W. & Michael, M. J. Carbon isotope stratigraphy of the Devonian of central and southern Europe. *Palaeogeogr. Palaeoclimatol. Palaeoecol.* **240**, 68–88 (2006).
32. Stolfus, B. M. et al. An expanded stratigraphic record of the Devonian–Carboniferous boundary Hangenberg biogeochemical event from southeast Iowa (USA). *Bull. Geosci.* **95**, 469–495 (2020).
33. Finlay, A. J., Selby, D. & Gröcke, D. R. Tracking the Hirnantian glaciation using Os isotopes. *Earth Planet. Sci. Lett.* **293**, 339–348 (2010).
34. Percival, L. M. E. et al. Pulses of enhanced continental weathering associated with multiple Late Devonian climate perturbations: evidence from osmium-isotope compositions. *Palaeogeogr. Palaeoclimatol. Palaeoecol.* **524**, 240–249 (2019).
35. Edmond, J. M. Himalayan tectonics, weathering processes, and the strontium isotope record in marine limestones. *Science* **258**, 1594–1597 (1992).
36. Garver, J. I., Royce, P. R. & Smick, T. A. Chromium and nickel in shale of the Taconic foreland; a case study for the provenance of fine-grained sediments with an ultramafic source. *J. Sediment. Res.* **66**, 100–106 (1996).
37. Hiscott, R. N. Ophiolitic source rocks for Taconic-age flysch: trace-element evidence. *Geol. Soc. Am. Bull.* **95**, 1261–1267 (1984).
38. Workman, R. K. & Stanley, R. H. Major and trace element composition of the depleted MORB mantle (DMM). *Earth Planet. Sci. Lett.* **231**, 53–72 (2005).

39. Viers, J., Dupré, B. & Gaillardet, J. Chemical composition of suspended sediments in world rivers: new insights from a new database. *Sci. Total Environ.* **407**, 853–868 (2009).
40. Farrell, U. C. et al. The sedimentary geochemistry and paleoenvironments project. *Geobiology* **19**, 545–556 (2021).
41. Broecker, W. S. & Peng, T.-H. *Tracers in the Sea* Vol. 690 (Lamont-Doherty Geological Observatory, Columbia Univ., 1982).
42. Bayon, G. et al. Accelerated mafic weathering in Southeast Asia linked to late Neogene cooling. *Sci. Adv.* **9**, eadf3141 (2023).
43. Rosenthal, Y. et al. Site U1482. In *Proceedings of the International Ocean Discovery Program*: *Western Pacific Warm Pool* Vol. 363 (eds Rosenthal, Y. et al.) (IODP, 2018); publications.iodp.org/proceedings/363/363.PDF
44. Kennedy, M. J. & Wagner, T. Clay mineral continental amplifier for marine carbon sequestration in a greenhouse ocean. *Proc. Natl Acad. Sci. USA* **108**, 9776–9781 (2011).
45. Kennedy, M., Droser, M., Mayer, L. M., Pevear, D. & Mrofka, D. Late Precambrian oxygenation; inception of the clay mineral factory. *Science* **311**, 1446–1449 (2006).
46. Schrag, D. P., Berner, R. A., Hoffman, P. F. & Halverson, G. P. On the initiation of a snowball Earth. *Geochem. Geophys. Geosyst.* https://doi.org/10.1029/2001GC000219 (2002).

Methods

Mineral weathering

The weathering of igneous minerals is simplified to a balanced chemical equation from primary mineral to its most common weathering product. We allow the secondary mineral to further weather if those reactions are commonly reported. We treat quartz, kaolinite and goethite as stable. In nature, weathering reactions are more complicated than represented here. For example, clays formed in weathering ophiolites can be found as purely smectite (often stevensite or montmorillonite)[17]; however, chlorite can be found interlayered with smectite, potentially formed during hydrothermal processes or as an intermediate weathering product[16]. To consider siliciclastic mineralogy on a global scale, we idealize the weathering of each mineral independently and ignore the influence of co-occurring species. The idealized weathering reactions for each mineral are given in the Supplementary Information, with discussions of the simplifications we have made. We use chemical compositions to convert modal abundances to mass fractions (Fig. 1).

Weathering rates depend not only on the mineralogy but also on climate and physical erosion rates. Fortunately, the ratio of weathering rates between different minerals has been shown to be broadly constant across laboratory and field experiments[20], allowing us to simplify our model and use only relative weathering rates. The ratio of mineral alteration rates is given in Supplementary Table 1. Our weathering model follows the progression of alteration reactions from primary to secondary (and tertiary where necessary), where the rate of the alteration of mineral A to mineral B is proportional to the inverse square root of the mean age of the reactant mineral[44]:

$$\mathrm{d}C_\mathrm{b}/\mathrm{d}t \propto k_\mathrm{a} C_\mathrm{a} \omega_\mathrm{a}^{-1/2} \tag{1}$$

where k_a is the rate ratio of mineral A (Supplementary Table 1), ω_a is the normalized age of mineral A, C_a is the fraction of mineral A present in the rock. We model the reaction numerically, updating the ages and concentrations of minerals A and B (and C where necessary). Because the weathering rates are constructed relative to one another and are not absolute, ω reflects a normalized age such that by $\omega = 1$, all reactions are complete and only silica, kaolinite, and goethite remain (Fig. 1); ω also serves as the degree of weathering in our carbon model (equations (10) and (12)).

We apply our weathering model to three igneous rock compositions: ultramafic, mafic and felsic. The mineralogy of those initial, igneous compositions is given in Supplementary Table 2. Mineral abundances are given as modal abundance and converted to mass to show chemical depletion. We then convert mass to SSA by the values in Supplementary Table 2. Primary minerals are assigned an SSA of 0.1 $\mathrm{m^2\,g^{-1}}$ except for serpentine, which is 8 $\mathrm{m^2\,g^{-1}}$ (ref. 47), and muscovite, which has an illite SSA of 80 $\mathrm{m^2\,g^{-1}}$ (ref. 48).

SSA–TOC relationship

To couple SSA to TOC, we derived an empirical relationship between the two. We compiled 483 analyses of both SSA and TOC in shales across four continents (Supplementary Table 6). Only those studies that used ethylene glycol monoethyl ether for SSA analyses were selected due to the ability of both internal and external surface area to preserve organic carbon. We seek a best-fit function of the form:

$$\mathrm{TOC} = a \times \mathrm{SSA}^b \tag{2}$$

However, b is close to 1 for most fit parameters, and as such we simplify our idealized relationship to a proportionality:

$$\mathrm{TOC} = a \times \mathrm{SSA} \tag{3}$$

The value of a is derived by a weighted linear regression of the SSA and TOC values in Supplementary Table 6. Weights are proportional to the sum of the normalized Euclidean distances between the sample point and all other points (equation (4)).

$$w_i \propto \sum \sqrt{\left(\frac{\mathrm{toc}_i - \mathrm{toc}_j}{\overline{\mathrm{toc}}}\right)^2 + \left(\frac{\mathrm{ssa}_i - \mathrm{ssa}_j}{\overline{\mathrm{ssa}}}\right)^2} \tag{4}$$

This yields $a = 0.0306$ g $\mathrm{m^{-2}}$, giving a function that maps from sediment SSA to TOC. This relationship is consistent with preservation approximately equivalent to monolayer loading of TOC on clays[11,44]. We show the data and best-fit line in Fig. 1e. We explore the dependence on our SSA–TOC relationship in Supplementary Fig. 15 using values of coefficients a and b.

While mineral protection is a major control on OC burial on the continental margin[11,13,14], treating TOC solely as a function of SSA is an oversimplification. We ignore here the effects of temperature, sedimentation rate and bottom-water oxygen concentration. High sedimentation rates can lower the time over which OC is exposed to oxygen, increasing preservation[11]. Similarly, ocean anoxia can reduce remineralization rates and raise TOC concentrations above monolayer equivalent values[44]. The effects of temperature on OC preservation may be a feedback that is not represented within our model. Cooling increases the solubility of oxygen within water, which could serve as a negative feedback by increasing remineralization rates at higher dissolved oxygen levels. Alternatively, respiration reactions slow considerably with lower temperature, which may act as a positive feedback. Our model serves only to isolate the effect of clay mineralogy and SSA over Earth's climate, rather than act as a complete model for sedimentation, ocean chemistry, redox and preservation on the continental margin.

We investigate the magnitude of changes induced by SSA-driven OC preservation using a simple one-box model that couples the global fraction of exposed felsic, mafic and ultramafic rocks to clay formation, silicate weathering and $p_{\mathrm{CO_2}}$. The formation of clays is governed by the preceding descriptions while all other relationships are simplified to power laws or Arrhenius relationships.

Carbon box model

Our model follows the work of ref. 9. The evolution of the mass of C in the ocean–atmosphere system, M_c, is a balance of influxes and outfluxes:

$$\Delta M_\mathrm{c}/\Delta t = F_\mathrm{v} - F_\mathrm{sw} - F_\mathrm{org} \tag{5}$$

where F_v is the flux of C from volcanic outgassing, metamorphic CO_2 release and organic carbon/pyrite weathering. Today, this value is poorly constrained. We choose 200 Mt $\mathrm{yr^{-1}}$ (for example, refs. 49–51).

F_sw is the flux of C from ocean–atmosphere to lithosphere due to the precipitation of carbonate minerals from silicate-derived cations. F_sw is a function of both lithology and $p_{\mathrm{CO_2}}$ according to equation (6):

$$F_\mathrm{sw} = k_\mathrm{sw} \times \lambda \times p_{CO_2}^{\beta} \tag{6}$$

where

$$\lambda = \text{weatherability} = p_\mathrm{f} + 3.1 \times p_\mathrm{m} + 8.1 \times p_\mathrm{u} \tag{7}$$

where $p_\mathrm{f}, p_\mathrm{m}, p_\mathrm{u}$ = protolith fraction of felsic, mafic and ultramafic rock, respectively; β = silicate weathering exponent = 0.22 (ref. 51); $k_\mathrm{sw} = 25$ Mt $\mathrm{yr^{-1}}$; k_sw is chosen such that $F_\mathrm{sw} \approx 0.65\,F_\mathrm{v}$ at pre-industrial conditions of $p_{\mathrm{CO_2}} = 280$ ppm and $\lambda = 1.06$.

Calculating $p_{\mathrm{CO_2}}$ requires assumptions about carbonate saturation in the ocean. Over the long timescales we consider here, we treat the sum of ocean [Mg] + [Ca] to be constant and assume that M_c is dominantly HCO_3^-. Given the residence time of Mg in the ocean is ~13 Myr, these simplifications are reasonable. However, our estimated changes in $p_{\mathrm{CO_2}}$ should be treated as approximations.

$$p_{CO_2}(t) = 280\ \text{ppm} \times \left(\frac{M_c(t)}{M_c(0)}\right)^2 \quad (8)$$

Where $M_c(0)$ is the mass of carbon in the modern ocean–atmosphere system, 38,600,000 Mt (ref. 9).

F_{org} is the burial of organic carbon, calculated according to equations (9)–(14). We consider only the sediments delivered to the continental margin and deltaic regions. F_{org} can be limited either by the supply of mineral surfaces or by the supply of phosphorus to the ocean, and we use the minimum of those two constraints in calculating F_{org}.

Today, two-thirds of modern sediment delivery is from the mafic, tectonically active regions that constitute southeast Asia and Oceania[52], suggesting that ophiolite obduction would increase global sedimentation rates. Conservatively, we assume that while the SSA of sediment changes, the total sediment flux remains constant. Similarly, we take ω to reflect mean global climate. In areas with high degrees of chemical weathering and low physical erosion rates, ω may be far greater than the global value, moving past $\omega = 10^{-3.6}$, at which point SSA and OC burial would begin to decrease, limiting the effect of obduction (Fig. 1 and Supplementary Fig. 1). Our model results do not reflect the increased local weathering in the warm, rainy tropics compared with higher latitudes[53], and the outsized importance of tropical lithologies is not incorporated[7,8,53].

$$F_{os} = d \times F_{sed} \times \text{TOC}/100 \quad (9)$$

$$\text{SSA} = p_f \times G_s(\omega) + 3.1 \times p_m \times B_s(\omega) + 8.1 \times p_u \times P_s(\omega) \quad (10)$$

$$F_{op} = 12 \times M_P \times \frac{\text{C/P}}{31} \quad (11)$$

F_{sed} = global sediment flux = 14030 MT/yr

d = nearshore/deltaic fraction of sediment flux = 0.3

F_{os} = SSA limited OC burial

F_{op} = Phosphorus limited OC burial

M_P = mass of available phosphorus in ocean

where F_{sed} = global sediment flux = 14,030 Mt yr^{-1} (ref. 54); d = nearshore/deltaic fraction of sediment flux = 0.3 (ref. 55); F_{os} = SSA-limited OC burial; F_{op} = phosphorus-limited OC burial; M_p = mass of available phosphorus in ocean; G_s, B_s and P_s are the numerical functions derived from mineral weathering laws that relate ω to SSA as described in the preceding and shown in Fig. 1d. TOC is linked to SSA via equation (2). The values of 3.1 and 8.1 that appear in equations (7) and (10) parameterize the silicate weathering rates of mafic and ultramafic rocks, relative to felsic rocks, derived from the molar abundance of Ca and Mg[38,56,57]. The constants 12 and 31 reflect the molar mass of carbon and phosphorus, respectively; ω is coupled to climate by the Arrhenius relationship (equation (12)), and temperature is approximated by a climate sensitivity equation (equation (13) (refs. 6,27,58)).

$$\omega = \omega_0\, e^{-\frac{E_a}{R}\left(\frac{1}{T}-\frac{1}{T_0}\right)} \quad (12)$$

$$T = T_0 + S\log_2(p_{CO2}/p_{CO2}(0)) \quad (13)$$

S = Climate sensitivity = 3 K

T_0 = pre − industrial average temperature = 298 K

$pCO_2(0)$ = pre − industrial pCO_2 = 280 ppm

E_a = activation energy = 74.9 kJ

R = gas constant = 8.314 kJ/K/mol

ω_0 = reference weathering degree = 10^{-4}

where S = climate sensitivity = 3 K (ref. 27); T_0 = pre-industrial average temperature = 298 K; $p_{CO_2}(0)$ = pre-industrial p_{CO_2} = 280 ppm; E_a = activation energy = 74.9 kJ (ref. 6); R = gas constant = 8.314 kJ K^{-1} mol^{-1}; ω_0 = reference weathering degree = 10^{-4}. We constrain ω_0 by compiling mineralogy from over 55,000 Deep Sea Drilling Project (DSDP) smear slides. By taking the mean modal mineralogy, we find that the terrigenous portion consists primarily of clays, silica, feldspar and iron oxides (Supplementary Fig. 16). The presence of 7.5% feldspar and 0.5% pyroxene places ω_o between 10^{-5} and 10^{-3}. We use 10^{-4} for the results presented in Fig. 2 and present a sensitivity test in Supplementary Fig. 17.

M_P is modelled similarly to M_C (equation (5)) but governed only by the riverine flux, F_{P_SW}, and OC burial divided by the buried C/P ratio.

$$F_{P\_SW} = 0.7 \times F_{sw} \times (31/12) \times (p_f \times 0.0111 + p_m \times 0.0071 \times 3.1 + p_u \times 0.00069 \times 8.1)/\lambda \quad (14)$$

$$F_{P\_OC} = F_{org}/\text{C/P} \times 31/12 \quad (15)$$

$$\text{C/P} = 106 + (\text{C/P}_{max} - 106) \times e^{-20\frac{M_P}{M_P(0)}} \quad (16)$$

The factor of 0.7 in equation (13) reflects the fraction of riverine phosphorus that is bioavailable (for example, refs. 59,60); the constants 0.0111, 0.0071 and 0.00069 are the molar ratios of P to Ca + Mg in felsic, mafic and ultramafic rocks, respectively; and e is Euler's number. In Fig. 2, we vary C/P_{max}. The value −20 in equation (15) is a decay constant designed to maintain the Redfield ratio outside of very low values of M_P (Supplementary Fig. 18). $M_P(0)$ is set as 1.2×10^5, derived from a steady-state OC burial of 70 Mt yr^{-1} and a residence time of 69,000 yr (ref. 41). Given our model's lack of negative feedbacks for high phosphorus concentrations, we artificially impose an upper limit of 2×10^5. Sedimentary deposits of phosphate, which are common in the rock record but minor in the modern ocean, provide a pathway by which excess phosphorus is removed from the ocean[61].

Assuming carbonate minerals precipitate without carbon isotopic fractionation, the $\delta^{13}C$ of the ocean–atmosphere system through time is controlled by the fluxes F_V and F_{org}, as well as the size of the carbon reservoir:

$$\Delta\delta^{13}C/\Delta t = 1/M \times ((F_V \times (\delta_V - \delta^{13}C)) - F_{org} \times \delta_{org}) \quad (17)$$

In equation (16), δ_V is the combined carbon isotopic ratio of volcanic outgassing (traditionally −5‰) and organic carbon weathering (traditionally −22‰), which we set constant at −9‰ to achieve a steady-state $\delta^{13}C$ around 0‰ (ref. 9). δ_{org} is the fractionation of carbon, relative to the oceanic value, via photosynthesis, which we hold at −25‰ (ref. 62).

Compilation of natural records

Mean $\delta^{13}C$ excursions were calculated from the chemostratigraphic sections in Supplementary Table 5 and are used in Fig. 3. The magnitude of each excursion was chosen by eye. Representative sections are displayed in Fig. 3b and Supplementary Fig. 2 and were chosen due to their age constraints and higher temporal resolution. Our model curves are scaled uniformly in time to qualitatively match the shown sections. We linearly interpolated ages of isotopic records between the known ages listed in Supplementary Table 4. The resultant time evolution is poorly constrained, with some sections tied only by two age estimates.

The Permo–Carboniferous $\delta^{13}C$ range is derived from the data of ref. 10. We used change-point analysis of a smoothed spline (smoothing parameter 0.1) through the data to find the onset of the $\delta^{13}C$ excursion at 324.4 Ma and plateau at 308.0 Ma. We subtract each $\delta^{13}C$ datum with age 324.4 ± 1 Ma (n = 30) from each $\delta^{13}C$ datum with age 308.0 ± 1 Ma (n = 70) and take the median and 1σ range of the resultant values.

We calculate the ophiolite length change for each glaciation by interpolating the suture lengths of ref. 8 at 0.1 Ma resolution and subtracting the pre-glacial and post-glacial suture lengths from the syn-glacial suture lengths. We use the ages of the glaciations given in Supplementary Table 3. For the suture lengths that follow the Permo–Carboniferous, we use 255 Ma as the minimum age.

Analysis of shale geochemistry

We queried the Stanford Geochemistry and Palaeoenvironments database[40], filtering for 'shale', 'mudstone', and 'siltstone' as the lithology. A total of 7,820 samples contained data for Cr, Al_2O_3 and TOC; 6,679 samples contained data for Co, Al_2O_3 and TOC; and 7,755 contained data for Ni, Al_2O_3 and TOC. We consider the ratio Cr/Al as a simple measure of ultramafic provenance. To make systematic variations more visible, we construct bins of Cr/Al and calculate the distribution of TOC within those bins. Any bin with fewer than 15 samples is ignored. In Fig. 4a, we show the median Cr/Al, the median TOC and the 1σ range in TOC values (16th to 84th quantiles). Figure 4b overlays the Phanerozoic time variation in shale Cr/Al on the abrupt and prolonged endmember glaciation chronologies (Supplementary Table 3). Similar relationships are shown in Supplementary Fig. 11 for Co/Al and Ni/Al.

Data availability

Compiled SSA and TOC data are available in Supplementary Table 6. Geologic constraints are available in Supplementary Table 7. SGP data were downloaded on 3 October 2022, filtering for the following lithologies: shale, mudstone, siltstone. Iron and phosphorus data were downloaded from EarthChem on 19 March 2022, filtering all igneous rock analyses for which SiO_2, FeO, and P_2O_5 are present. The igneous and sedimentary geochemical data are reproduced within the Supplementary Data and are available at https://doi.org/10.6084/m9.figshare.24433012.

Code availability

MATLAB functions are available for both the weathering model, weatherRock.m, and the carbon box model, carbonPhosphorusModel.m. The functions can be found at https://doi.org/10.6084/m9.figshare.24433012.

References

47. Rivero Crespo, M. A., Pereira Gómez, D., Villa García, M. V., Gallardo Amores, J. M. & Vicente, S. E. Characterization of serpentines from different regions by transmission electron microscopy, X-ray diffraction, BET specific surface area and vibrational and electronic spectroscopy. *Fibers* **7**, 47 (2019).
48. Young, R. *Soil Properties and Behaviour* Vol. 5 (Elsevier, 2012).
49. Burton, M. R., Georgina, M. S. & Granieri, D. Deep carbon emissions from volcanoes. *Rev. Mineral. Geochem.* **75**, 323–354 (2013).
50. Soulet, G. et al. Temperature control on CO_2 emissions from the weathering of sedimentary rocks. *Nat. Geosci.* **14**, 665–671 (2021).
51. Berner, R. A., Lasaga, A. C. & Garrels, R. M. Carbonate-silicate geochemical cycle and its effect on atmospheric carbon dioxide over the past 100 million years. *Am. J. Sci.* **283**, 641–683 (1983).
52. Milliman, J. D. & Farnsworth, K. L. *River Discharge to the Coastal Ocean: A Global Synthesis* (Cambridge Univ. Press, 2013).
53. Kent, D. V. & Muttoni, G. Modulation of Late Cretaceous and Cenozoic climate by variable drawdown of atmospheric p_{CO_2} from weathering of basaltic provinces on continents drifting through the equatorial humid belt. *Climate* **9**, 525–546 (2013).
54. Syvitski, J. P. M., Charles, J. V., Kettner, A. J. & Green, P. Impact of humans on the flux of terrestrial sediment to the global coastal ocean. *Science* **308**, 376–380 (2005).
55. Kuehl, S. A., Mead, A. A., Goodbred, S. L. & Kudrass, H. N. *The Ganges–Brahmaputra Delta* (SEPM, 2005).
56. Rudnick, R. L. & Gao, S. in *Treatise on Geochemistry* Vol. 3 (eds Holland, H. D. & Turekian, K. K.) 1–64 (Elsevier, 2003).
57. Gale, A., Colleen, A. D., Charles, H. L., Su, Y. & Schilling, J. -G. The mean composition of ocean ridge basalts. *Geochem. Geophys. Geosyst.* **14**, 489–518 (2013).
58. Arrhenius, S. XXXI. On the influence of carbonic acid in the air upon the temperature of the ground. *Lond. Edinb. Dublin Phil. Mag. J. Sci.* **41**, 237–276 (1896).
59. Stepanauskas, R. et al. Summer inputs of riverine nutrients to the Baltic Sea: bioavailability and eutrophication relevance. *Ecol. Monogr.* **72**, 579–597 (2002).
60. Pacini, N. & Gächter, R. Speciation of riverine particulate phosphorus during rain events. *Biogeochemistry* **47**, 87–109 (1999).
61. Frohlich, P. N., Bender, M. L., Luedtke, N. A., Heath, G. R. & DeVries, T. The marine phosphorus cycle. *Am. J. Sci.* **282**, 474–511 (1982).
62. Hayes, J. M., Strauss, H. & Kaufman, A. J. The abundance of ^{13}C in marine organic matter and isotopic fractionation in the global biogeochemical cycle of carbon during the past 800 Ma. *Chem. Geol.* **161**, 103–125 (1999).

Acknowledgements

We thank D. Rothman and F. Macdonald for their insight, particularly in respect to the carbon cycle and its isotopic record. We thank M. Follows for a valuable discussion on dissolved oxygen and remineralization. Funding for this work came from NSF EAR 1925863.

Author contributions

J.M. and O.J. conceptualized the research. J.M. led modelling and statistical methods. J.M. and O.J. were responsible for data analysis, writing and editing.

Competing interests

The authors declare no competing interests.

Additional information

Supplementary information The online version contains supplementary material available at https://doi.org/10.1038/s41561-023-01342-9.

Correspondence and requests for materials should be addressed to Joshua Murray.

Peer review information *Nature Geoscience* thanks Donald Penman, Thomas Blattmann and Germain Bayon for their contribution to the peer review of this work. Primary Handling Editors: James Super and Alison Hunt, in collaboration with the *Nature Geoscience* team.